ACS Photonics

pubs.acs.org/journal/apchd5

Article

Topological Valley Transport of Terahertz Phonon–Polaritons in a $LiNbO_3$ Chip

Hao Xiong, Yao Lu,* Qiang Wu,* Zhixuan Li, Jiwei Qi, Xitan Xu, Ruobin Ma, and Jingjun Xu*

Cite This: https://doi.org/10.1021/acsphotonics.1c00860

Read Online

ACCESS | Metrics & More | Article Recommendations | Supporting Information

ABSTRACT: Topological photonics has thrived in various optical systems over the past decade for the fascinating properties of eliminating backscattering losses and enhancing the efficiency of communication systems. The demonstration of topology in strong light–matter coupling regimes may prove tunable optical devices that are immune to disorder and defects or achieve the extreme light confinement. Recently, the topological properties of exciton–polaritons were experimentally studied in deep cryogenic temperatures. As for another elementary quasiparticle in solids, phonon–polaritons, which can remain stable at a high temperature, the relative topological dispersion contours have been observed very recently at room temperatures. Here, we experimentally presented a topological valley transport of terahertz phonon–polaritons in $LiNbO_3$ photonic crystal slab. Topological waveguides with two peculiar interfaces are designed and studied, where the phonon–polaritons are generated through femtosecond laser pulses. We show the intensity distribution and dispersion curves of phonon–polaritons propagating in the topological waveguides at different bended interfaces, in which the topological edge modes make smooth detours. Our work opened a new path toward topological polaritonics at a valley-edge-mode based phonon–polariton platform, which also provides insights to the low loss phonon–polariton chips, strong light–matter interactions, nonlinear topological photonics, and future THz communications.

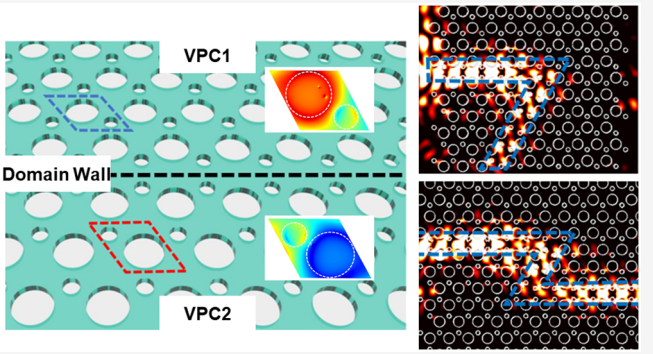

KEYWORDS: *topological valley transport, terahertz phonon–polaritons, $LiNbO_3$, chip, edge states*

Topological photonics has drawn huge attentions since the concept was proposed,[1,2] because light waves can serve as a platform to investigate nontrivial bulk and edge physics which are robust against defects or backscattering. Over the past decade, much effort has been dedicated to achieving topological edge states through metamaterials[3−11] or photonic crystals.[12−23] These studies include time-reversal breaking systems using either magnetic fields or synthetic gauge fields,[11,24,25] as well as time-reversal conserved systems based on quantum spin Hall effect (QSH)[12,13,23,26,27] or quantum valley Hall effect (QVH)[19−22,28,29] without magnetic components or temporal modulation. These developments mostly focused on the linear optical effects, while applications in photonic circuitry often require nonlinear optical properties.[30] Topological polaritons,[31] first proposed by T. Karzig, which combine the topology and light–matter nonlinear interactions, have made considerable achievements in topological polaritonics.[32−36] Different from bare photonic systems, the polaritonic systems could induce strong interparticle interactions and enhance the sensitivity to external stimuli, which are helpful to assembling the nonlinear and actively controllable topological devices.[36] Currently, the studies on topological polaritons mainly concentrate on the exciton–polariton systems, with the corresponding experiments demanding deep cryogenic temperature and strong magnetic fields. Recently, topological polaritons have been demonstrated in an analogous QSH system by strongly coupling excitons with a topologically nontrivial hexagonal photonic crystal at 200 Ks without external magnetic fields, where the nontrivial topology originates from the pseudospin of the lattice. However, phonon–polaritons, as another elementary polariton in solid state systems,[37−39] could remain stable, even at room temperatures or high temperatures. Therefore, the realization of topological phonon–polaritons may enable the topological control over the ionic crystals.

Research on phonon–polaritons mainly include two regimes, one in the van der Waals materials[40,41] and the other in the bulk ionic crystals,[42−44] based on the material they are explored in. In very recent studies, the topological transition of phonon–polaritons in twisted stacks of two-

Received: June 12, 2021

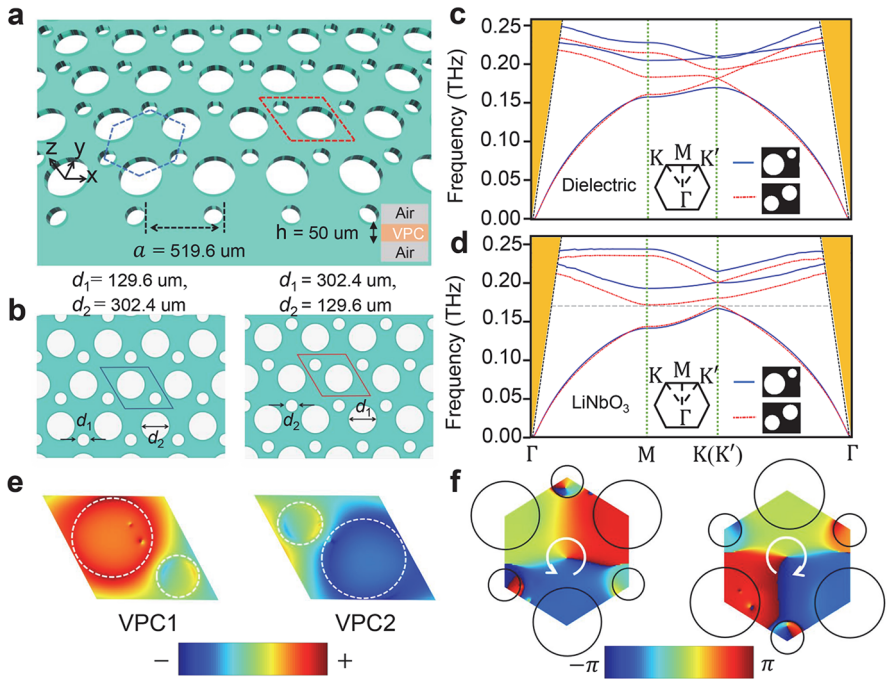

Figure 1. $LiNbO_3$ on-chip VPCs and nontrivial properties in its band diagram. (a) Schematic of the $LiNbO_3$ VPC structure in oblique view. The blue dashed hexagon shows the unit cell and the red rhombus represents the Wigner−Seitz cell. The VPC is built on a 50 μm $LiNbO_3$ crystal chip with lattice constant a = 519.6 μm. Inset shows the symmetric construction of the VPC in the z direction. (b) Details of the Wigner−Seitz cell of two different VPCs, which is composed of two inequivalent air holes, with the diameter of the larger one being 302.4 μm and the smaller one being 129.6 μm. While the blue rhombus indicates the Wigner−Seitz cell of VPC1 (d_1 = 129.6 μm, d_2 = 302.4 μm), the red rhombus represents the Wigner−Seitz cell of VPC2 (d_1 = 302.4 μm, d_2 = 129.6 μm). (c, d) Band structures with and without inversion symmetry for an isotropic dielectric chip (n = 6.4) and a $LiNbO_3$ chip (see detailed information in the Supporting Information), respectively. The red line represents the dispersion diagram with inversion symmetry and the blue line indicates the other. Golden-color regions in (c) and (d) represent the light cone of isotropic dielectric material and $LiNbO_3$ crystal. (e) Mode profiles in the first band at the K valley for VPC1 and VPC2 ($LiNbO_3$), respectively. The color scale represents the z-oriented field H_z. (f) Phase vortex of the H_z profile in the first band at the K valley for VPC1 and VPC2 ($LiNbO_3$), respectively. The H_z phase vortex generally rotates around the center of the unit cell, corresponding to left or right circularly polarized (LCP or RCP) distribution. The field patterns are collected at the z = 0 plane.

dimensional materials (such as α-MoO_3)[45,46] and gratings[47] were experimentally studied, but the topological edge transport of phonon−polaritons in the ionic crystals still remains a fertile ground to be explored. Currently, the high loss in transmission caused by the backscattering of microstructures and material defects significantly hindered the development of the phonon−polariton systems. In addition, some crucial techniques that have been generally applied in optics and photonics, such as effective propagation control and attenuation minimization of phonon−polaritons, are still not available, significantly hindering the further applications of the polaritonic platforms. Fortunately, the introduction of the topological edge transport of phonon−polaritons can provide potential solutions to these problems. Significantly, it can further enhance the light−matter interaction, so as to achieve a more extreme light confinement. Furthermore, implementing topological edge states in phonon−polariton systems may also enable the topological control over the lattices,[43] which could help to construct topological optomechanical systems,[48] light-induced heating systems[49] and light-induced phase-transition systems[50,51] via the nonlinear effects brought by phonon−polaritons.

In this work, we experimentally presented a topological valley transport of phonon−polaritons by constructing an analogous QVH system based on the $LiNbO_3$ photonic crystal slab. This is the first time demonstrating topological valley edge modes of phonon−polaritons experimentally, to the best of our knowledge. The propagation of phonon−polaritons in the topological waveguides with bended interfaces was recorded through a phase-contrast imaging technique. The intensity distributions of topological edge states for phonon−polaritons are displayed, in which the edge modes bypassed the 120° bends smoothly. The valley photonic crystals (VPCs) applied in the experiment were fabricated through femtosecond laser direct writing technique. This work provides an integrated platform for the combination of phonon−polaritons and topological edge states, which is not only rather intriguing in topological transmission control over phonon−polaritons, but also promising in extreme light confinement, topologically integrated polaritonics, and future THz communications.

Phonon Polaritons and the Master Equation. Phonon polaritons are one of the most important quasiparticles in ionic crystals, which are ultrastrong coupling states of the photons and optical phonons. They are equipped with the ability to confine light into the deep subwavelength scale, and thus, show a great potential in enhancing light−matter interactions in the infrared and THz range.[52−54] In this case, the Hamiltonian of this coupling system can be written as[55]

$$\hat{H} = \hbar\omega_0\hat{\sigma}^{\dagger}\sigma + \hbar\omega_{ph}\hat{a}^{\dagger}\hat{a} + \frac{\hbar\Omega}{2}(\hat{\sigma}^{\dagger} + \hat{\sigma})(\hat{a}^{\dagger} + \hat{a}) \quad (1)$$

where the first two terms indicate the Hamiltonian of optical phonons and THz photons, and the last term depicts the coupling between them. The creation/annihilation operators for the optical phonons with frequency ω_0 and photons with

https://doi.org/10.1021/acsphotonics.1c00860
ACS Photonics XXXX, XXX, XXX−XXX

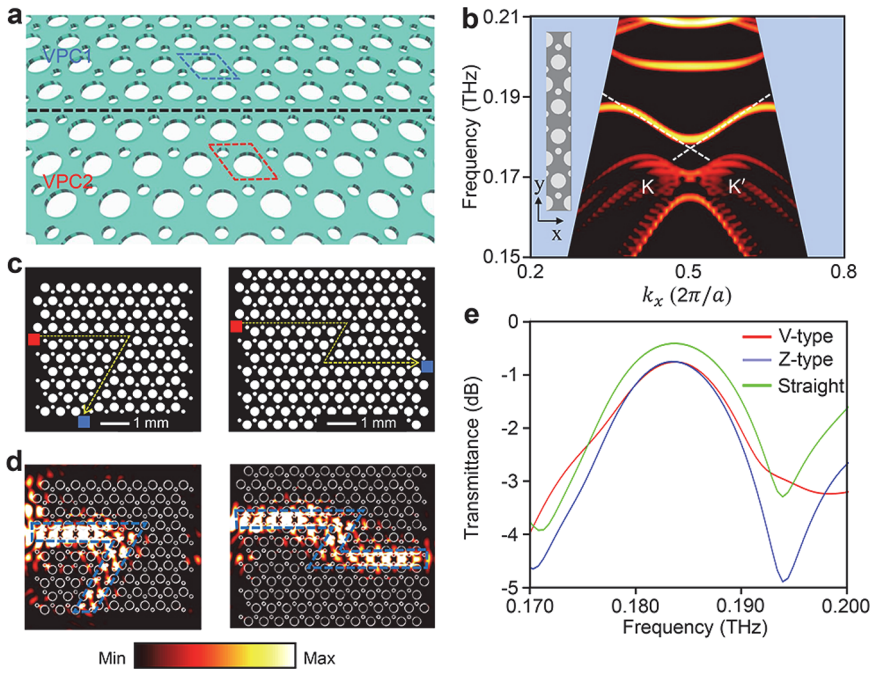

Figure 2. Topological Edge states at the domain wall between VPC1 and VPC2. (a) Schematic of the domain wall constructed by VPC1 and VPC2. The black dashed line indicates location of the domain wall. The red and blue rhombi represent the unit cell of VPC1 and VPC2, respectively. (b) Dispersion diagram of the supercell shown in the inset which is periodic in the x direction and finite in the y direction (10 unit cells of each region). The supercell has a thickness of 50 μm in the z direction, which is in accordance with the VPCs design. Shading region: light cone of $LiNbO_3$ crystal. (c) The V-type and Z-type photonic crystals with a "V" shape and "Z" shape interface between VPC1 and VPC2. The red and blue rectangles indicate input and output sides of the VPCs, respectively. The yellow dashed lines show the paths of two interfaces. (d) Intensity distribution of the propagating valley edge states for V-type and Z-type photonic crystals at the frequency f = 0.184 THz which locates in the bandgap. (e) Transmission spectra of the VPCs with two different shapes of interfaces shown in (b) and a straight interface (shown in (a) with 12 unit cells) as a comparison.

frequency ω_{ph} are represented by $(\hat{\sigma}^\dagger, \hat{\sigma})$ and $(\hat{a}^\dagger, \hat{a})$, respectively. Simultaneously, as a type of quasiparticle, Hamiltonian of the phonon−polariton can also be represented by its creation and annihilation operators $(\hat{\xi}^\dagger, \hat{\xi})$

$$\hat{H} = \hbar\omega\hat{\xi}^\dagger\hat{\xi} \tag{2}$$

with the creation/annihilation operators satisfy $[\hat{\xi}, \hat{\xi}^\dagger] = 1$, and $[\hat{\xi}, \hat{H}] = \hbar\omega\hat{\xi}$. Apparently, both eq 1 and eq 2 describe the phonon−polaritons, but with different representations: coupling representation and polariton representation, respectively. Here, we expand the operator $\hat{\xi}$ in coupling representation, which reads

$$\hat{\xi} = \alpha\hat{a} + \beta\hat{\sigma} + \gamma\hat{a}^\dagger + \delta\hat{\sigma}^\dagger \tag{3}$$

In eq 3, the coefficients α, β, γ, and δ represent the projections of operator $\hat{\xi}$ in the four basis vectors. To further deduce these four coefficients, we calculate the commutation $[\hat{\xi}, \hat{H}]$ in both representations. Through the comparison between the results in the two different representations, we can get the necessary conditions for the existence of phonon−polaritons, shown as follows (the detailed calculation is shown in Supporting Information):

$$\omega^4 - \omega^2(\omega_0^2 + \omega_{ph}^2) + \omega_{ph}^2\omega_0^2 + 4\Omega^2\omega_0\omega_{ph} = 0 \tag{4}$$

By taking the following substitutions, $\omega_{ph}^2 = \varepsilon_\infty c^2k^2$ and $4\Omega^2 = \omega_0\omega_{ph}\left(1 - \frac{\varepsilon_0}{\varepsilon_\infty}\right)$, we can solve and obtained the contribution of phonon−polaritons, shown as follows:

$$\varepsilon(\omega) = \varepsilon_\infty + \frac{\omega_0^2(\varepsilon_0 - \varepsilon_\infty)}{\omega_0^2 - \omega^2} \tag{5}$$

In eq 5, ε_0 and ε_∞ are the low- and high-frequency dielectric constants of the material for $LiNbO_3$ crystals, respectively. Considering the vibration of ionic crystals will introduce loss to the dielectric constant, a damping efficient γ is introduced to eq 5, which gives

$$\varepsilon(\omega) = \varepsilon_\infty + \frac{\omega_0^2(\varepsilon_0 - \varepsilon_\infty)}{\omega_0^2 - \omega^2 + i\omega\gamma} \tag{6}$$

Considering the Maxwell equations, the Master equation for phonon−polariton crystals should be

$$\frac{1}{\varepsilon(\omega, \vec{r})}\nabla \times [\nabla \times E(\vec{r})] = \frac{\omega^2}{c^2}E(\vec{r}) \tag{7}$$

For a periodic structure, $\varepsilon(\omega, \vec{r} + \vec{R}) = \varepsilon(\omega, r)$, the electric field satisfies the Bloch conditions $E(\omega, \vec{r} + \vec{R}) = E(\omega, \vec{r})e^{i\vec{k}\cdot\vec{R}}$, and the band theory can thus be used in phonon−polariton crystals. In the following simulations, the dielectric constant $\varepsilon(\omega)$ in eq 6 is considered for the phonon−polaritons in $LiNbO_3$ crystals and applied in the material setup.

Design of the on-Chip Phonon−Polariton VPCs. In this work, VPCs at THz wavelengths are fabricated on an x-cut $MgO/LiNbO_3$ slab waveguide with a thickness of h = 50 μm, as depicted in Figure 1a. The honeycomb-like lattice is adopted here to form two kinds of VPCs with the same lattice constant a = 519.6 μm. Figure 1b shows details of the VPCs, where the unit cell of VPC1 (blue rhombus) is composed of two

https://doi.org/10.1021/acsphotonics.1c00860
ACS Photonics XXXX, XXX, XXX−XXX

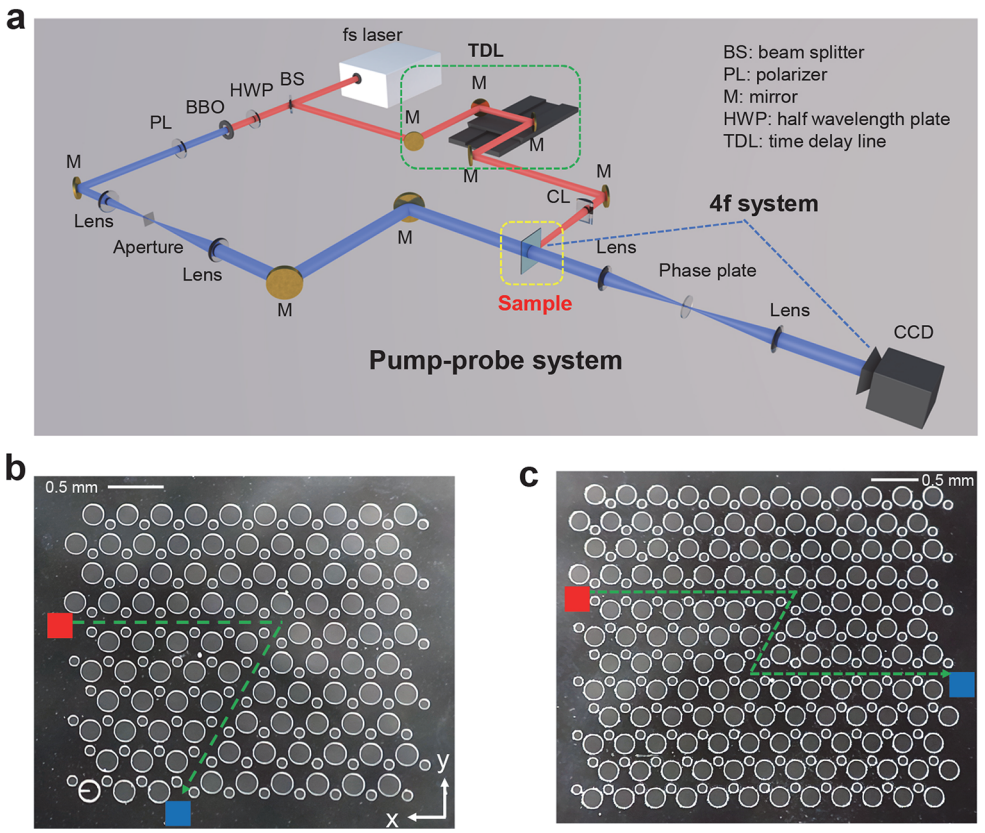

Figure 3. Experimental setup and the fabricated $LiNbO_3$ VPCs. (a) Schematic of the experimental setup (pump−probe detecting system) used for generating and detecting phonon−polaritons. The pump beam is 800 nm presented by the red light and the probe beam is 400 nm, indicated by the blue light. Components in the green dashed box represent the time delay line and the yellow dashed box shows location of the $LiNbO_3$ sample, after which follows a standard 4f imaging system. (b, c) Photos of the V-type (b) and Z-type VPCs (c) we fabricated on $LiNbO_3$ chips. Red and blue rectangles show where the phonon−polaritons are imported and exported, the green dashed line indicates the interface between VPC1 and VPC2, respectively.

distinctive air holes. The diameter of the smaller one is d_1 = 129.6 μm and the larger one is d_2 = 302.4 μm. On the contrary, the diameter of the two air holes exchanged to construct another type of VPC, that is, VPC2 (red rhombus) with d_1 = 302.4 μm and d_2 = 129.6 μm. Considering that VPC2 is the inversion symmetry partner of VPC1, they thus share the same band structure.

As for a standard honeycomb lattice, each unit cell contains two identical circular holes with diameters $d_1 = d_2$. In this case we mainly concentrate on the transverse-electric (TE) modes where electric fields lie within the plane. Because of the total internal reflection, the TE modes propagate in the xy plane and are restricted in the z direction. The C_6 symmetry of the photonic crystal lattice leads to the emergence of a Dirac cone at the $K(K')$ points in the momentum space, shown by the red curves in Figure 1c. Varying the diameters of the two air holes in the unit cell to make $d_1 \neq d_2$ reduces the lattice symmetry from C_6 to C_3, which breaks the inversion symmetry. Inversion symmetry breaking lifts the degeneracy at the Dirac point and thus forms a band gap, as shown by the blue curves in Figure 1c. It is worth noting that the $LiNbO_3$ slab applied here is anisotropic, which results in the disappearance of the Dirac cone in the standard honeycomb case, but a complete bandgap still appears after the inversion symmetry was broken, as shown in Figure 1d. We should note that the introduction of anisotropy will render an inequivalence among three K/K' in the Brillouin zone, and finally leads to a deviation in the band diagram. Here, considering the modification brought by anisotropy does not affect the opening and closing of the topological bandgap, we take the K/K' points marked in Figure 1d as a representation for simplicity.

As the unit cell is deformed to two nonequivalent air holes, the $LiNbO_3$ VPCs open a large TE-like band gap (0.175−0.195 THz) indicated by the blue curves in Figure 1d. Figure 1e shows the distribution of the H_z mode profile in the first band at the K valley for VPC1 and VPC2 ($LiNbO_3$), respectively, from which two different modes could be seen. Then the H_z phase vortex profile at the K valley in the first band is calculated as plotted in Figure 1f, from which we could see that the phase vortex profile of VPC1/VPC2 increases anticlockwise/clockwise by a 2π phase around the center of a unit cell, exhibiting left or right circularly polarized distribution. Such an optical vortex is related to a valley pseudospin in an electronic system, which could be termed as a photonic valley degree of freedom and related to a topologically nontrivial phase.[21] The H_z mode profile and phase vortex profile present opposite circularly polarized modes at the K valleys of VPC1 and VPC2, indicating a valley-chirality locking property. As a result, VPC1 and VPC2 are assigned with the opposite Chern number at the K/K' valley.[21]

Numerical Simulations. Valley-dependent edge states are generally demonstrated at the interface between two VPCs with a reversed unit cell because the different signs of the

https://doi.org/10.1021/acsphotonics.1c00860
ACS Photonics XXXX, XXX, XXX−XXX

Chern number will guarantee the protection of the topological valley phase.[21,22,28] Based on the results above, a domain wall between VPC1 and VPC2 is constructed to realize the topological valley transport, as depicted in Figure 2a, where the interface is stacked with the smaller holes as the black dashed line shows. The dispersion curves along the interface are calculated and shown in Figure 2b, where the valley-dependent edge states exhibit a negative group velocity at the K valley but a positive one at the K/K' valley. In addition, edges states near the valleys show a linear dispersion even though the edge dispersion does not gaplessly cross from the lower band to the upper band. Then we constructed two topological interfaces with one and two bends respectively, shown in Figure 2c as V-type and Z-type, to observe the robust valley transport in the simulation. THz phonon−polaritons emit from the input into the interface of topological waveguide marked by the red rectangle, and propagated along the interfaces toward the output of topological waveguide marked by the blue rectangle. The simulated results of the intensity distribution in Figure 2d confirms smooth detours in both cases with the 120° turn. Furthermore, the edge states propagate through the sharp corners with negligible refection, which is an evidence to the robustness of topological edge states. With the incident THz phonon−polaritons being broadband ranging from 0.150−0.210 THz, transmission spectra at the outputs of V-type and Z-type waveguides are shown by red and blue curves in Figure 2e, respectively. To make a comparison, the transmission spectrum for a straight topological interface is calculated and shown by the green curve in Figure 2e. It is evident that the transmission peak occurs in the band gap of the dispersion diagram. The maximum point in the spectrum for straight, V-type and Z-type waveguide is close to each other in both location and amplitude, once again proves the robustness of edge states against the extra bend. It is worth mentioning that anisotropy of the material will also impact the range of the edge states in the bandgap. Therefore, the topological phonon−polaritons that are permitted propagating at the interface of different angles to the y axis will not perfectly superstition. Topological phonon−polaritons collected at the output side will thus be an intersection of the topological edge states that coexist at different interfaces.

EXPERIMENTAL RESULTS

To achieve the topological valley transport of THz phonon−polaritons experimentally, we fabricated the topological waveguides based on the 10 mm × 11 mm × 50 μm $LiNbO_3$ wafers using the femtosecond laser direct writing technology.[56] (More details of the fabrication can be seen in the Supporting Information.)

Especially, the $LiNbO_3$ chip we applied here not only serves as the carrier of VPCs waveguide, but also a tiny emitting source of THz phonon−polaritons under the irradiation of 800 nm femtosecond laser. The pump−probe experimental setup is schematically displayed in Figure 3a.[57,58] The femtosecond laser is split into two branches through a beam splitter. The probe branch is frequency-doubled by a BBO crystal and then expanded to illuminate the whole $LiNbO_3$ VPCs, and the pump branch is line-focused through a cylindrical lens as a source which radiates THz phonon−polaritons at the input end of VPCs. Different from the traditional method[58] to generate phonon−polaritons by directly injecting the focused femtosecond laser perpendicular to the $LiNbO_3$ chip, here we adopted a lateral excitation scheme[59,60] where the pump beam is parallel focused into the lateral side of the $LiNbO_3$ sample (see details in the Supporting Information). This scheme allows for the generation of THz phonon−polaritons in a narrow frequency range, which ensures a more focused energy distribution of the signals. Photos of V-type and Z-type $LiNbO_3$ VPCs applied in experiments are (xy view) shown in Figure 3b and c, respectively.

Figure 4a shows the laterally stimulated phonon−polaritons propagating in the $LiNbO_3$ waveguide outside the region of

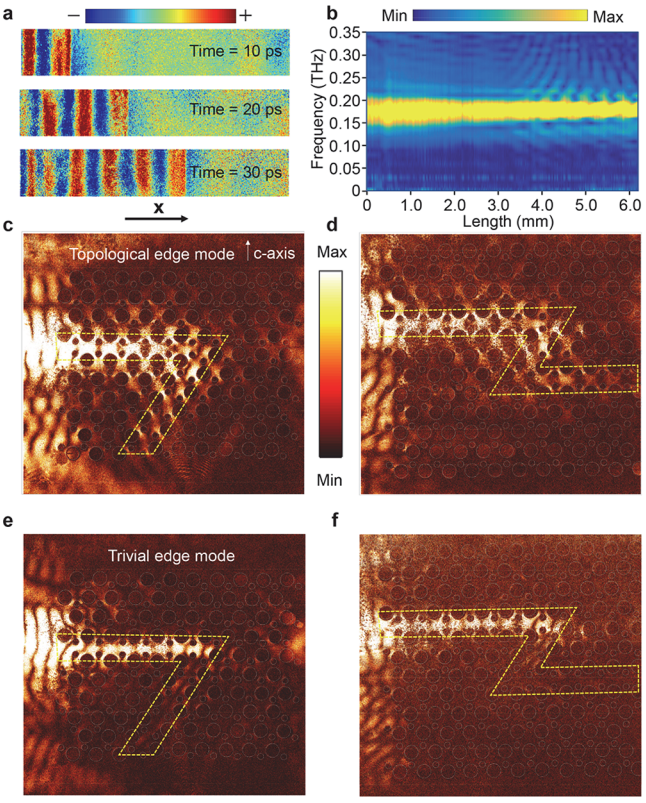

Figure 4. Observation of the topological valley transport for THz phonon−polaritons. (a) Electric field distribution of phonon−polaritons generated in the $LiNbO_3$ waveguide by lateral excitation outside the air hole lattice district at three different time (10, 20, and 30 ps). The propagation direction is along the x-axis, which is vertical to the c-axis of $LiNbO_3$. (b) The $x-f$ map, which represents the frequency spectrum for phonon−polaritons propagating along the x-axis. (c, d) Intensity distribution of the phonon−polaritons stimulated inside the bandgap at 0.190 THz (inside the topological bandgap) in the V- and Z-type VPCs. Yellow dashed sections display energy density distribution at the interface. (e, f) Intensity distribution of the trivial phonon−polaritons stimulated outside the bandgap at 0.210 THz (outside the topological bandgap) in the V- and Z-type VPCs.

patterned airholes, and the corresponding electric field distribution at different times is recorded. As the time goes from 10 to 30 ps, phonon−polaritons in the waveguide transport vertically to the c-axis with a relatively stable field distribution. Variations of the frequency spectrum for phonon−polaritons along the x axis (propagating direction) are shown in Figure 4b, where the generated phonon−polaritons mainly fall into the frequency range between 0.150−0.200 THz, which covers the bandgap we have calculated above.

Using this technique, the phonon−polaritons are generated at the input end of the $LiNbO_3$ VPCs through lateral excitation

https://doi.org/10.1021/acsphotonics.1c00860
ACS Photonics XXXX, XXX, XXX−XXX

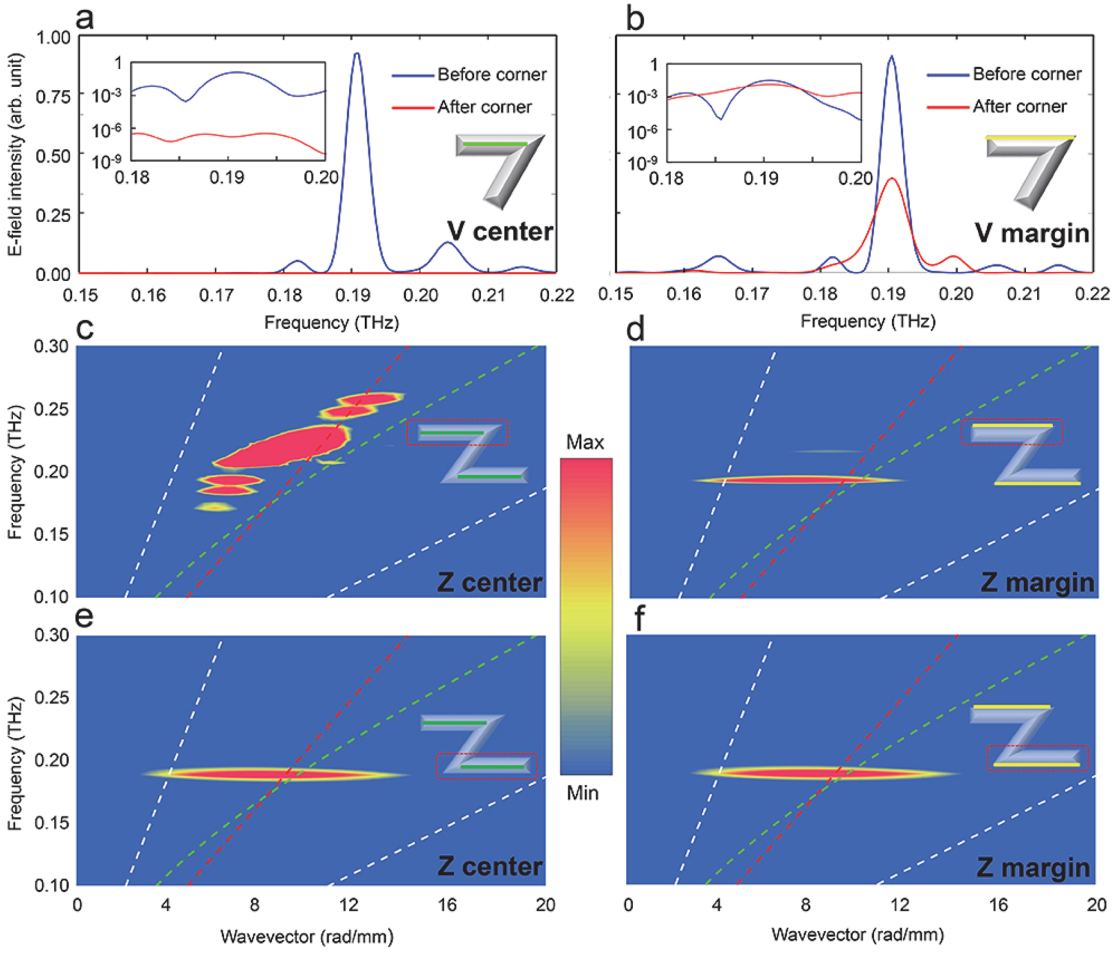

Figure 5. Propagating features of topological phonon−polaritons along the interface. (a, b) Spectra at the center and margin of the interface before and after the first corner in the V-type waveguide, respectively. Insets: The exponential coordinates of (a) and (b) from 0.18 to 0.20 THz. (c, e) Dispersion curves along center of the top and bottom edge in the Z-type waveguide, respectively. The white dashed line indicates the light cone of the $LiNbO_3$ slab, and the green and red dashed line represents the fundamental mode and femtosecond laser in the $LiNbO_3$ slab, respectively. (d, f) Dispersion curves along margin of the top and bottom edge in the Z-type waveguide, respectively.

and then enter the waveguide and propagate along the interface. The intensity distributions of the phonon−polaritons at different frequencies for both V- and Z-type waveguides are measured and plotted. Figure 4c,d shows the intensity distributions of phonon−polaritons at 0.190 THz (inside the topological bandgap) in V- and Z-type waveguides, respectively. At this frequency, after the phonon−polaritons entered the VPCs, the majority of them propagated along the interface between the topologically distinctive regions. When encountered with the first wide angle bend (120°), the topologically protected THz phonon−polaritons bypassed the corner successfully in both V- and Z-type waveguides and made smooth detours along the interface. Furthermore, phonon−polaritons in the Z-type waveguide even propagated around the second bend smoothly, which showed great potential in the propagation control of phonon−polaritons. Instead, when we calculated the energy distributions of phonon−polariton edge modes at 0.210 THz (outside the topological bandgap) in V- and Z-type waveguides, the results are different, shown in Figure 4e and f, respectively. Distinguished from the topological case, phonon−polaritons at this frequency propagated along the interface until the very first bend, where most of them were scattered in different directions and the rest of the few kept traveling along the trajectory, exhibiting a trivial transport behavior.

In addition, when compared with the trivial case, the topological phonon−polaritons showed a wider intensity distribution which covered the margin of the interface (where the yellow dashed line locates in Figure 3b,c) before the first sharp turn. As for the trivial mode, the intensity distribution mainly centered within the region between the two small face-to-face air holes, the center of the interface (where the green dashed line is located in Figure 3b,c). After encountering the first sharp corner, as shown in Figure 4c,d, the energy distribution of the topological phonon−polaritons experienced a morphological variation from taking up the whole interface to the margin of the interface, while phonon−polaritons were propagating toward the lower left direction. To better elaborate this point, the spectra at the center and margin of the interface before and after the sharp turn in Figure 4c are calculated as shown in Figure 5a,b. The intensity of topological phonon−polaritons at the center of the interface experienced a huge drop after the sharp turn, which is 5 orders of magnitude smaller than before the corner at 0.190 THz, as shown in Figure 5a. Differently, the intensity of topological phonon−polaritons at the margin of the interface maintained a

https://doi.org/10.1021/acsphotonics.1c00860
ACS Photonics XXXX, XXX, XXX−XXX

considerable value after the sharp corner, which stays in the same order of magnitude compared with before the corner.

Furthermore, to better study features of the topological phonon−polaritons as it traveled along the topological interface, we first calculated dispersion curves in the Z-type waveguide along center of the interface at the top edge and bottom edge, as shown in Figure 5c and e, respectively. At the top edge of the waveguide, THz phonon−polaritons distributed within a wide range in the spectrum, shown in Figure 5c, where there is a big part of energy distribution outside the topological bandgap. Unlike the bulk states below 0.170 THz, phonon−polaritons between 0.205 to 0.235 THz featured strong direction along the interface like we have shown in Figure 4e,f, rather than propagating into the bulk region. At the bottom edge of the waveguide, after the two sharp corners, phonon−polaritons are highly concentrated at the frequency around 0.190 THz inside the topological bandgap, shown in Figure 5e. Then we calculated the dispersion curves along margin of the interface, as shown in Figure 5d,f. In this case, phonon−polaritons at the top edge were limited in the topological bandgap with a high concentration around 0.190 THz, as shown in Figure 5d. Trivial modes outside the topological bandgap were filtered at the beginning. Correspondingly, the distribution of phonon−polaritons at the bottom edge was focused around 0.190 THz as shown in Figure 5f, which exhibited a good consistency with it at the top edge.

The phonon−polariton modes excited in $LiNbO_3$ featured a strong propagating direction vertical to the *c*-axis for their anisotropic characteristics, and thus induced a large loss efficient along the *y*-axis in our experiment. These results above demonstrated the topological protected THz phonon−polaritons stimulated in the $LiNbO_3$ chip when encountered with bended interfaces, and showed a good agreement with the simulation.

CONCLUSION

To conclude, we achieved the topological edge modes of phonon−polaritons in the $LiNbO_3$-based photonic crystal chip that exhibits valley Hall effect at THz wavelengths. To the best of our knowledge, this is the first time to experimentally demonstrate the topological edge states of phonon−polaritons. Topological phonon−polaritons are generated in the V-type and Z-type topological waveguides that are designed and fabricated on the $LiNbO_3$ chip through femtosecond laser direct writing technique. The intensity distribution and dispersion curves of the edge modes propagating in the bended interfaces with sharp turns are displayed, where topological phonon−polaritons make smooth detours when encountered with wide angle (120°) bends while the trivial ones are majorly scattered. This work paves the way to the topological control over phonon−polaritons in solids based on an analogous QVH system at a phonon−polariton chip. Compared with the traditional silicon-based chips, the $LiNbO_3$ slab offers the possibility of ultrafast optical modulation with low insertion loss based on the Pockels effect,[61] which provides a valuable platform to achieve and manipulate the topological polaritons for its large nonlinearity. Implementing topological photonic crystals in anistropical materials also provides insights for the modification of topological band gap and, thus, to control topological transport in the photonic-crystal waveguides from another perspective. A demonstration of topological edge states of phonon−polaritons in such a highly integrated platform that combines the generation, manipulation, and detection in a single chip is promising for applications of on-chip topological devices such as splitters, routing, and delay lines. Besides, our scheme gives a new solution to realize the THz topological edge states rather than using a THz laser machine, owing to the special frequency range covered by phonon−polaritons. The extreme light confining properties brought by topological phonon−polaritons could also enhance the sensitivity of the photonic system to external stimuli, which is rather intriguing when it comes to the THz sensing and THz integrated circuits. Furthermore, the construction of topological edge states in the phonon−polariton system may enable the topological control over the lattices, which has great potential in building topological optomechanic systems, light-induced heating systems and light-induced phase transition systems through the nonlinear effects brought by phonon−polaritons.

METHODS

Sample Fabrication. The topological VPCs composed of air holes are manufactured on a 50 μm thickness $LiNbO_3$ slab by the femtosecond laser direct writing technique. To prevent the sample from the sputtering materials during the fabrication, the $LiNbO_3$ slab was precovered with a 2 μm SiO_2 film on the surfaces. First, patterns of the VPCs are programmed in LabView, which controlled the movement of the three-dimensional translation table. Second, the $LiNbO_3$ slab was ablated by an 800 nm femtosecond laser beam (with its repetition frequency 1 kHz and power 10 mW), which was focused by an objective lens. After the ablation, the $LiNbO_3$ slab was etched in the 40% HF liquid for 30 min to remove the protection film on the surfaces.

Experimental Setup. The experimental results of the generated THz phonon−polaritons in the topological VPCs are realized with a femtosecond laser centered at 800 nm. In the experimental setup, a pump−probe system was applied with the pump beam being 800 nm and the probe beam being 400 nm. The pump beam was focused by a cylinder and radiated at the input of the VPCs to generate THz phonon−polaritons, while the probe beam was expanded and radiated on the facet of the whole $LiNbO_3$ sample to record the phase shift caused by phonon−polaritons through an electro-optic effect. The information on the phase shift could then be transformed to intensity information by a 4f imaging system and then collected by a CCD camera, which is also known as the phase-contrast imaging technique. The spatiotemporal evolution of phonon−polaritons in the $LiNbO_3$ could be recorded by moving the delay line between the pump and probe beams.

Numerical Simulation. All of the simulation results (the bulk/edge band structures, mode profiles, field distributions, and transmission spectra) in this work were calculated in three-dimensional (3D) simulations using finite-difference time-domain (FDTD) software. The source set in the band structure calculations is randomly distributed transverse electric dipoles. The intensity distributions of the edge modes at the interfaces are performed in time domain with a linear polarized dipole source at the input.

ASSOCIATED CONTENT

Supporting Information

The Supporting Information is available free of charge at https://pubs.acs.org/doi/10.1021/acsphotonics.1c00860.

https://doi.org/10.1021/acsphotonics.1c00860
ACS Photonics XXXX, XXX, XXX−XXX

Derivation of the phonon−polariton dispersion relations, material setup of the valley polaritonic crystal in FDTD, and generation and detection of the THz phonon−polaritons in $LiNbO_3$. (PDF)

AUTHOR INFORMATION

Corresponding Authors

Yao Lu − *The Key Laboratory of Weak-Light Nonlinear Photonics, Ministry of Education, TEDA Institute of Applied Physics and School of Physics, Nankai University, Tianjin 300457, China;* orcid.org/0000-0002-3687-4848; Email: yaolu@nankai.edu.cn

Qiang Wu − *The Key Laboratory of Weak-Light Nonlinear Photonics, Ministry of Education, TEDA Institute of Applied Physics and School of Physics, Nankai University, Tianjin 300457, China; Collaborative Innovation Center of Extreme Optics, Shanxi University, Taiyuan, Shanxi 030006, China;* orcid.org/0000-0003-3189-2219; Email: wuqiang@nankai.edu.cn

Jingjun Xu − *The Key Laboratory of Weak-Light Nonlinear Photonics, Ministry of Education, TEDA Institute of Applied Physics and School of Physics, Nankai University, Tianjin 300457, China; Collaborative Innovation Center of Extreme Optics, Shanxi University, Taiyuan, Shanxi 030006, China;* Email: jjxu@nankai.edu.cn

Authors

Hao Xiong − *The Key Laboratory of Weak-Light Nonlinear Photonics, Ministry of Education, TEDA Institute of Applied Physics and School of Physics, Nankai University, Tianjin 300457, China*

Zhixuan Li − *The Key Laboratory of Weak-Light Nonlinear Photonics, Ministry of Education, TEDA Institute of Applied Physics and School of Physics, Nankai University, Tianjin 300457, China*

Jiwei Qi − *The Key Laboratory of Weak-Light Nonlinear Photonics, Ministry of Education, TEDA Institute of Applied Physics and School of Physics, Nankai University, Tianjin 300457, China; Collaborative Innovation Center of Extreme Optics, Shanxi University, Taiyuan, Shanxi 030006, China*

Xitan Xu − *The Key Laboratory of Weak-Light Nonlinear Photonics, Ministry of Education, TEDA Institute of Applied Physics and School of Physics, Nankai University, Tianjin 300457, China*

Ruobin Ma − *The Key Laboratory of Weak-Light Nonlinear Photonics, Ministry of Education, TEDA Institute of Applied Physics and School of Physics, Nankai University, Tianjin 300457, China*

Complete contact information is available at: https://pubs.acs.org/10.1021/acsphotonics.1c00860

Notes

The authors declare no competing financial interest.

ACKNOWLEDGMENTS

This work is supported by the National Natural Science Foundation of China (11974192 and 11874229), the Foundation of State Key Laboratory of Laser Interaction with Matter (SKLLIM1903), the Basic Research Project (2020-JCJQ-ZD-120-00), the 111 Project (B07013), and the Program for Changjiang Scholars and Innovative Research Team in University (IRT_13R29).

REFERENCES

(1) Raghu, S.; Haldane, F. D. M. Analogs of quantum-Hall-effect edge states in photonic crystals. *Phys. Rev. A: At., Mol., Opt. Phys.* **2008**, *78*, 033834.

(2) Haldane, F.; Raghu, S. Possible realization of directional optical waveguides in photonic crystals with broken time-reversal symmetry. *Phys. Rev. Lett.* **2008**, *100*, 013904.

(3) Ma, T.; Khanikaev, A. B.; Mousavi, S. H.; Shvets, G. Guiding electromagnetic waves around sharp corners: topologically protected photonic transport in metawaveguides. *Phys. Rev. Lett.* **2015**, *114*, 127401.

(4) Gao, W.; Lawrence, M.; Yang, B.; Liu, F.; Fang, F.; Béri, B.; Li, J.; Zhang, S. Topological photonic phase in chiral hyperbolic metamaterials. *Phys. Rev. Lett.* **2015**, *114*, 037402.

(5) Mousavi, S. H.; Khanikaev, A. B.; Wang, Z. Topologically protected elastic waves in phononic metamaterials. *Nat. Commun.* **2015**, *6*, 8682.

(6) Chen, W. J.; Jiang, S. J.; Chen, X. D.; Zhu, B.; Zhou, L.; Dong, J. W.; Chan, C. T. Experimental realization of photonic topological insulator in a uniaxial metacrystal waveguide. *Nat. Commun.* **2014**, *5*, 5782.

(7) Gomez-Diaz, J. S.; Tymchenko, M.; Alu, A. Hyperbolic plasmons and topological transitions over uniaxial metasurfaces. *Phys. Rev. Lett.* **2015**, *114*, 233901.

(8) Cheng, X.; Jouvaud, C.; Ni, X.; Mousavi, S. H.; Genack, A. Z.; Khanikaev, A. B. Robust reconfigurable electromagnetic pathways within a photonic topological insulator. *Nat. Mater.* **2016**, *15*, 542−548.

(9) Yves, S.; Fleury, R.; Berthelot, T.; Fink, M.; Lemoult, F.; Lerosey, G. Crystalline metamaterials for topological properties at subwavelength scales. *Nat. Commun.* **2017**, *8*, 16023.

(10) Krishnamoorthy, H. N.; Jacob, Z.; Narimanov, E.; Kretzschmar, I.; Menon, V. M. Topological transitions in metamaterials. *Science* **2012**, *336*, 205−209.

(11) Wang, Z.; Chong, Y.; Joannopoulos, J. D.; Soljačić, M. Observation of unidirectional backscattering-immune topological electromagnetic states. *Nature* **2009**, *461*, 772−775.

(12) Wu, L.-H.; Hu, X. Scheme for achieving a topological photonic crystal by using dielectric material. *Phys. Rev. Lett.* **2015**, *114*, 223901.

(13) Barik, S.; Miyake, H.; DeGottardi, W.; Waks, E.; Hafezi, M. Two-dimensionally confined topological edge states in photonic crystals. *New J. Phys.* **2016**, *18*, 113013.

(14) Lu, L.; Fang, C.; Fu, L.; Johnson, S. G.; Joannopoulos, J. D.; Soljačić, M. Symmetry-protected topological photonic crystal in three dimensions. *Nat. Phys.* **2016**, *12*, 337−340.

(15) Xiong, H.; Wu, Q.; Lu, Y.; Wang, R.; Zhang, Q.; Qi, J.; Yao, J.; Xu, J. Polarization-resolved edge states in terahertz topological photonic crystal. *Opt. Express* **2019**, *27*, 22819−22826.

(16) Mukherjee, S.; Spracklen, A.; Valiente, M.; Andersson, E.; Öhberg, P.; Goldman, N.; Thomson, R. R. Experimental observation of anomalous topological edge modes in a slowly driven photonic lattice. *Nat. Commun.* **2017**, *8*, 13918.

(17) Milićević, M.; Ozawa, T.; Montambaux, G.; Carusotto, I.; Galopin, E.; Lemaître, A.; Le Gratiet, L.; Sagnes, I.; Bloch, J.; Amo, A. Orbital edge states in a photonic honeycomb lattice. *Phys. Rev. Lett.* **2017**, *118*, 107403.

(18) Weimann, S.; Kremer, M.; Plotnik, Y.; Lumer, Y.; Nolte, S.; Makris, K. G.; Segev, M.; Rechtsman, M. C.; Szameit, A. Topologically protected bound states in photonic parity−time-symmetric crystals. *Nat. Mater.* **2017**, *16*, 433−438.

(19) Ma, T.; Shvets, G. All-Si valley-Hall photonic topological insulator. *New J. Phys.* **2016**, *18*, 025012.

(20) Yang, Y.; Gao, Z.; Xue, H.; Zhang, L.; He, M.; Yang, Z.; Singh, R.; Chong, Y.; Zhang, B.; Chen, H. Realization of a three-dimensional photonic topological insulator. *Nature* **2019**, *565*, 622−626.

(21) He, X. T.; Liang, E. T.; Yuan, J. J.; Qiu, H. Y.; Chen, X. D.; Zhao, F. L.; Dong, J. W. A silicon-on-insulator slab for topological valley transport. *Nat. Commun.* **2019**, *10*, 872.

(22) Shalaev, M. I.; Walasik, W.; Tsukernik, A.; Xu, Y.; Litchinitser, N. M. Robust topologically protected transport in photonic crystals at telecommunication wavelengths. *Nat. Nanotechnol.* **2019**, *14*, 31−34.
(23) Gao, X.; Yang, L.; Lin, H.; Zhang, L.; Li, J.; Bo, F.; Wang, Z.; Lu, L. Dirac-vortex topological cavities. *Nat. Nanotechnol.* **2020**, *15*, 1012−1018.
(24) Rechtsman, M. C.; Zeuner, J. M.; Plotnik, Y.; Lumer, Y.; Podolsky, D.; Dreisow, F.; Nolte, S.; Segev, M.; Szameit, A. Photonic Floquet topological insulators. *Nature* **2013**, *496*, 196−200.
(25) Skirlo, S. A.; Lu, L.; Igarashi, Y.; Yan, Q.; Joannopoulos, J.; Soljačić, M. Experimental observation of large Chern numbers in photonic crystals. *Phys. Rev. Lett.* **2015**, *115*, 253901.
(26) Barik, S.; Karasahin, A.; Flower, C.; Cai, T.; Miyake, H.; DeGottardi, W.; Hafezi, M.; Waks, E. A topological quantum optics interface. *Science* **2018**, *359*, 666−668.
(27) Zhu, X.; Wang, H.-X.; Xu, C.; Lai, Y.; Jiang, J.-H.; John, S. Topological transitions in continuously deformed photonic crystals. *Phys. Rev. B: Condens. Matter Mater. Phys.* **2018**, *97*, 085148.
(28) Yang, Y.; Yamagami, Y.; Yu, X.; Pitchappa, P.; Webber, J.; Zhang, B.; Fujita, M.; Nagatsuma, T.; Singh, R. Terahertz topological photonics for on-chip communication. *Nat. Photonics* **2020**, *14*, 446−451.
(29) Zeng, Y.; Chattopadhyay, U.; Zhu, B.; Qiang, B.; Li, J.; Jin, Y.; Li, L.; Davies, A. G.; Linfield, E. H.; Zhang, B.; Chong, Y.; Wang, Q. J. Electrically pumped topological laser with valley edge modes. *Nature* **2020**, *578*, 246−250.
(30) Bardyn, C. E.; Karzig, T.; Refael, G.; Liew, T. Topological polaritons and excitons in garden-variety systems. *Phys. Rev. B: Condens. Matter Mater. Phys.* **2015**, *91*, 161413.
(31) Karzig, T.; Bardyn, C.-E.; Lindner, N. H.; Refael, G. Topological polaritons. *Phys. Rev. X* **2015**, *5*, 031001.
(32) Wang, B.; Zhao, C. Topological phonon polaritons in one-dimensional non-Hermitian silicon carbide nanoparticle chains. *Phys. Rev. B: Condens. Matter Mater. Phys.* **2018**, *98*, 165435.
(33) St-Jean, P.; Goblot, V.; Galopin, E.; Lemaître, A.; Ozawa, T.; Le Gratiet, L.; Sagnes, I.; Bloch, J.; Amo, A. Lasing in topological edge states of a one-dimensional lattice. *Nat. Photonics* **2017**, *11*, 651−656.
(34) Nalitov, A.; Solnyshkov, D.; Malpuech, G. Polariton Z topological insulator. *Phys. Rev. Lett.* **2015**, *114*, 116401.
(35) Klembt, S.; Harder, T. H.; Egorov, O. A.; Winkler, K.; Ge, R.; Bandres, M. A.; Emmerling, M.; Worschech, L.; Liew, T. C. H.; Segev, M.; Schneider, C.; Hofling, S. Exciton-polariton topological insulator. *Nature* **2018**, *562*, 552−556.
(36) Liu, W.; Ji, Z.; Wang, Y.; Modi, G.; Hwang, M.; Zheng, B.; Sorger, V. J.; Pan, A.; Agarwal, R. Generation of helical topological exciton-polaritons. *Science* **2020**, *370*, 600−604.
(37) Huang, K. Lattice vibrations and optical waves in ionic crystals. *Nature* **1951**, *167*, 779−780.
(38) Huang, K. On the interaction between the radiation field and ionic crystals. *Proceedings of the Royal Society of London. Series A. Mathematical and Physical Sciences* **1951**, *208*, 352−365.
(39) Feurer, T.; Stoyanov, N. S.; Ward, D. W.; Vaughan, J. C.; Statz, E. R.; Nelson, K. A. Terahertz polaritonics. *Annu. Rev. Mater. Res.* **2007**, *37*, 317−350.
(40) Low, T.; Chaves, A.; Caldwell, J. D.; Kumar, A.; Fang, N. X.; Avouris, P.; Heinz, T. F.; Guinea, F.; Martin-Moreno, L.; Koppens, F. Polaritons in layered two-dimensional materials. *Nat. Mater.* **2017**, *16*, 182−194.
(41) Basov, D.; Fogler, M.; De Abajo, F. G. Polaritons in van der Waals materials. *Science* **2016**, *354*, aag1992−aag1992.
(42) Sivarajah, P.; Steinbacher, A.; Dastrup, B.; Lu, J.; Xiang, M.; Ren, W.; Kamba, S.; Cao, S.; Nelson, K. A. THz-frequency magnon-phonon-polaritons in the collective strong-coupling regime. *J. Appl. Phys.* **2019**, *125*, 213103.
(43) Lu, Y.; Zhang, Q.; Wu, Q.; Chen, Z.; Liu, X.; Xu, J. Giant enhancement of THz-frequency optical nonlinearity by phonon polariton in ionic crystals. *Nat. Commun.* **2021**, *12*, 3183.
(44) Lu, Y.; Wu, Q.; Zhang, Q.; Wang, R.-D.; Zhang, B.; Zhao, W.-J.; Zhang, D.; Xiong, H.; Yang, C.-L.; Qi, J.-W.; Pan, C.-P.; Xu, J.-J. Time-resolved imaging of mode-conversion process of terahertz transients in subwavelength waveguides. *Frontiers of Physics* **2019**, *14*, 42502.
(45) Hu, G.; Ou, Q.; Si, G.; Wu, Y.; Wu, J.; Dai, Z.; Krasnok, A.; Mazor, Y.; Zhang, Q.; Bao, Q.; Qiu, C.-W.; Alu, A. Topological polaritons and photonic magic angles in twisted α-MoO_3 bilayers. *Nature* **2020**, *582*, 209−213.
(46) Chen, M.; Lin, X.; Dinh, T. H.; Zheng, Z.; Shen, J.; Ma, Q.; Chen, H.; Jarillo-Herrero, P.; Dai, S. Configurable phonon polaritons in twisted α-MoO 3. *Nat. Mater.* **2020**, *19*, 1307−1311.
(47) Li, P.; Hu, G.; Dolado, I.; Tymchenko, M.; Qiu, C.-W.; Alfaro-Mozaz, F. J.; Casanova, F.; Hueso, L. E.; Liu, S.; Edgar, J. H.; Velez, S.; Alu, A.; Hillenbrand, R. Collective near-field coupling and nonlocal phenomena in infrared-phononic metasurfaces for nano-light canalization. *Nat. Commun.* **2020**, *11*, 3663.
(48) Mathew, J. P.; del Pino, J.; Verhagen, E. Synthetic gauge fields for phonon transport in a nano-optomechanical system. *Nat. Nanotechnol.* **2020**, *15*, 198−202.
(49) Kato, S.; Kurimura, S.; Mio, N. Rate-equation model of light-induced heating in LiNbO 3-type crystals under high-average-power laser irradiation. *Opt. Mater. Express* **2016**, *6*, 396−401.
(50) Ashida, Y.; İmamoğlu, A.; Faist, J.; Jaksch, D.; Cavalleri, A.; Demler, E. Quantum electrodynamic control of matter: Cavity-enhanced ferroelectric phase transition. *Phys. Rev. X* **2020**, *10*, 041027.
(51) Li, X.; Qiu, T.; Zhang, J.; Baldini, E.; Lu, J.; Rappe, A. M.; Nelson, K. A. Terahertz field−induced ferroelectricity in quantum paraelectric SrTiO3. *Science* **2019**, *364*, 1079−1082.
(52) Caldwell, J. D.; Glembocki, O. J.; Francescato, Y.; Sharac, N.; Giannini, V.; Bezares, F. J.; Long, J. P.; Owrutsky, J. C.; Vurgaftman, I.; Tischler, J. G.; Wheeler, V. D.; Bassim, N. D.; Shirey, L. M.; Kasica, R.; Maier, S. A. Low-loss, extreme subdiffraction photon confinement via silicon carbide localized surface phonon polariton resonators. *Nano Lett.* **2013**, *13*, 3690−3697.
(53) Alfaro-Mozaz, F. J.; Alonso-Gonzalez, P.; Velez, S.; Dolado, I.; Autore, M.; Mastel, S.; Casanova, F.; Hueso, L. E.; Li, P.; Nikitin, A. Y.; Hillenbrand, R. Nanoimaging of resonating hyperbolic polaritons in linear boron nitride antennas. *Nat. Commun.* **2017**, *8*, 15624.

https://doi.org/10.1021/acsphotonics.1c00860
ACS Photonics XXXX, XXX, XXX−XXX